




# A numerical investigation of three-dimensional falling liquid films

Lyes Kahouadji<sup>1</sup> · Assen Batchvarov<sup>1</sup> · Idris T. Adebayo<sup>1</sup> · Zachary Jenkins<sup>1</sup> · Seungwon Shin<sup>2</sup> · Jalel Chergui<sup>3</sup> · Damir Juric<sup>3,4</sup> · Omar K. Matar<sup>1</sup> 

Received: 27 October 2021 / Accepted: 26 February 2022 / Published online: 24 March 2022  
© The Author(s) 2022

## Abstract

In this article, we present a full three-dimensional numerical study of thin liquid films falling on a vertical surface, by solving the full three-dimensional Navier–Stokes equations with a hybrid front-tracking/level-set method for tracking the interface. General falling film flow applications span across many types of process industries but also occur in a multitude of natural and environmental applications such as ice sheets, glaciology and even volcanic lava flows. In this study, we propose three configurations of falling films. Two of them, with small and moderate Reynolds number, are set to mimic pulsed and forced falling film types inside a minimum periodic domain, able to cover entirely the temporal evolution of a single wave. The latest example, corresponding to a high Reynolds number, is initialised with a flat interface without any specific perturbations. For the first time, this study highlights the natural transition from a non-deformed interface to its first streamwise disturbance (two-dimensional wavy flow), and then a second spanwise wave disturbance (three-dimensional wavy flow).

**Keywords** Falling films · Direct numerical simulations · Multiphase flows · Front-tracking

## 1 Introduction

The flow of thin liquid films constitutes a very interesting research topic in fluid dynamics. This is in part due to their wide presence in numerous applications [16, 22] which include cooling, condensation, evaporation, and adsorption processes etc. It also comes with the advantage of intensified heat and mass transfer rates provided by the wavy

---

✉ Omar K. Matar  
o.matar@imperial.ac.uk

<sup>1</sup> Department of Chemical Engineering, Imperial College London, SW7 2AZ London, UK

<sup>2</sup> Department of Mechanical and System Design Engineering, Hongik University, Seoul 04066, Republic of Korea

<sup>3</sup> Centre National de la Recherche Scientifique (CNRS), Laboratoire Interdisciplinaire des Sciences du Numérique (LISN), Université Paris Saclay, 91400 Orsay, France

<sup>4</sup> Department of Applied Mathematics and Theoretical Physics, Centre for Mathematical Sciences, University of Cambridge, Wilberforce Road, Cambridge CB3 0WA, UK

structure of these films, even at relatively low liquid flow rates or short contact time between the liquid and solid wall [2, 14, 15].

Liquid falling films also occur broadly throughout nature and we can observe their presence in many geophysical settings [16]. For example, the modelling of ice sheets and glaciology, where the top layer of ice melts to form an inclined thin falling film, and leading to “wavy” ice formations rather than smooth streams [5, 6, 8]. Furthermore, understanding roll waves formed in mud as the result of the complex liquid rheology in a viscoplastic falling film can help predict intermittent surges in flooded rivers and flumes [7]. In fact, viscous falling films occur extensively throughout the study of debris flows and natural slurries [5] and are even involved in the modelling of lava domes [4, 16].

The dynamics of falling films can also be found throughout biological systems [16]. Within pulmonary science, falling films occur when mucus coats the airway walls where the thickness of these films have knock on effects to the opening and closing of the airways, as well as the transport of liquid into the lungs [20]. They also occur in other flexible tubes within the body, for example in the capillaries of the cardiovascular system, where a critical film-thickness to tube-radius ratio is required in order to effectively move blood around the body [21]. Finally, thin falling films play a critical role in human eyes, where a thin film of corneal fluid forms over the spherical surface of our own eye [16]. The understanding of these films is of the utmost importance, and could assist in the development of many everyday aids, such as soft contact lenses [37].

Due to the applications highlighted above, many efforts have been applied in fundamental research since the initial work of Kapitza and Kapitza [23] who have studied for the first time the evolution of waves on thin films. A Reynolds number  $Re$  based on an initial liquid height is a principal parameter to initialise and to predict the outcome regime flow [3, 10, 11, 13, 23–27, 32, 33, 36, 39, 40]. Liu et al. [25, 26] were able to highlight the development of large-amplitude solitary waves, known as gamma II waves, and also secondary instabilities following the initial bifurcation from a steady flat film. Their results have revealed the evolution of structured patterns, i.e. “herringbone”, from two-dimensional waves due to a subharmonic instability, and a synchronous three-dimensional pattern arising from a sideband type of instability. Park and Nosoko [32] have conducted remarkable experiments where they perturb the flow periodically. A temporal perturbation in the streamwise direction and the introduction of a spanwise disturbance caused by needles put in contact with the film’s free surface. With this type of experimental setup, they were able to obtain a critical perturbation wavelength for the solitary wave instability. Nosoko et al. [28] also investigated the characteristics of waves on thin films while deriving correlations for the dependence of both wave speed and peak height on the wavelength as well as film  $Re$  and  $We$  numbers. Further research efforts include the works of Kofman et al. [24], Dietze et al. [18] and Nosoko and Miyara [29]. Detailed reviews of several of these studies has also been carried out [13, 16] as well as a number of textbooks authored in this field [3, 13, 22].

On the mathematical modelling work front, initial work on the linear stability analyses of the base state of thin films was first carried out by Yih [39, 40] and Benjamin [10]. Their results showed the base state of the film to be unstable to long-wavelength disturbances. Consequently, further studies focused on the development of simplified equations from the full Navier–Stokes by a long-wave approximation and with different order-of-magnitude assumptions for the important  $Re$  and  $We$  numbers [11, 36]. The wave behaviour has still not been fully understood since these theoretical studies are only possible in the framework of linear stability analysis, which is limited to the initial stage of wave inception and very small  $Re$  values. Efforts have also been made on the solution of the non-linear equations. However the

analytical solutions are always limited to trivial cases, hence the need to focus on numerical solutions.

There are several attempts of computing falling films with different numerical approaches but most of them are within a two-dimensional numerical framework. Miyara [27] used a two-dimensional direct numerical simulation approach with a simplified Marker and Cell method. Ramaswamy et al. [33] have used finite element method with an Eulerian–Lagrangian formulation, while Gao [19] used Volume of Fluid (VOF) method with a Continuum Surface force for surface tension. Finally, Yu et al. [41], Xie et al. [38] and Adebayo et al. [1] have used an algebraic VOF formulation combined with an unstructured, anisotropic and adaptive meshes. Recently, Batchvarov et al. [9] performed the first three-dimensional computational study of vertical falling films in the presence of insoluble surfactants, interfacial active-agents, using similar configurations proposed by Dietze et al. [18]. Both studies [9, 18] have set a numerical domain restricted to only a single wave with periodic boundary conditions.

In summary, many of these above-mentioned studies have considered only two-dimensional configurations of the falling film problem. Though these provide a wide range of information as to the dynamics of the wave evolution process, it must be noted that the interface topology usually exhibits important spanwise features which are impossible to observe in the two dimensional plane. A far more abundant amount of information can be discovered in a three-dimensional analysis. Though three-dimensional simulations of falling films provide more realistic scenarios than a two-dimensional analysis, the complexity of the problem and the often large computational requirements have been impediments to wide-spread application. In this study, we present results of full three-dimensional direct numerical simulations of thin falling film flows.

## 2 Problem formulation, governing equations and numerical scheme

The mathematical model of the falling film configuration consists of two incompressible and immiscible viscous fluids in a three-dimensional domain  $\mathbf{x} = (x, y, z) \in [0, \lambda_x] \times [0, \lambda_y] \times [0, \lambda_z]$  (see Fig. 1) the governing equation are:

$$\nabla \cdot \mathbf{u} = 0 \quad (1)$$

$$\rho \left( \frac{\partial \mathbf{u}}{\partial t} + \mathbf{u} \cdot \nabla \mathbf{u} \right) = -\nabla p + \rho \mathbf{g} + \nabla \cdot \mu (\nabla \mathbf{u} + \nabla \mathbf{u}^T) + \mathbf{F} \quad (2)$$

where  $\mathbf{u} = (u, v, w)$  is the velocity vector,  $p$  the pressure,  $\mathbf{g} = (g, 0, 0)$  the gravitational acceleration vector directed towards the  $x$ -direction, and  $\mathbf{F}$ , the local surface tension force at the interface and defined by a hybrid formulation:

$$\mathbf{F} = \sigma \mathcal{K}_H \nabla \mathcal{H} \quad (3)$$

$\sigma$  refers to the surface tension coefficient.  $\mathcal{H}$  is a Heaviside function used here as a phase indicator, with a value of zero in the air phase and a value of one in the liquid phase, and is resolved with a sharp but smooth transition across 3–4 Eulerian grid cells.  $\mathcal{K}_H$  is twice the mean interface curvature field and is calculated on the Eulerian grid by:

$$\mathcal{K}_H = \frac{\mathbf{F}_L \cdot \mathbf{G}}{\sigma \mathbf{G} \cdot \mathbf{G}} \quad (4)$$

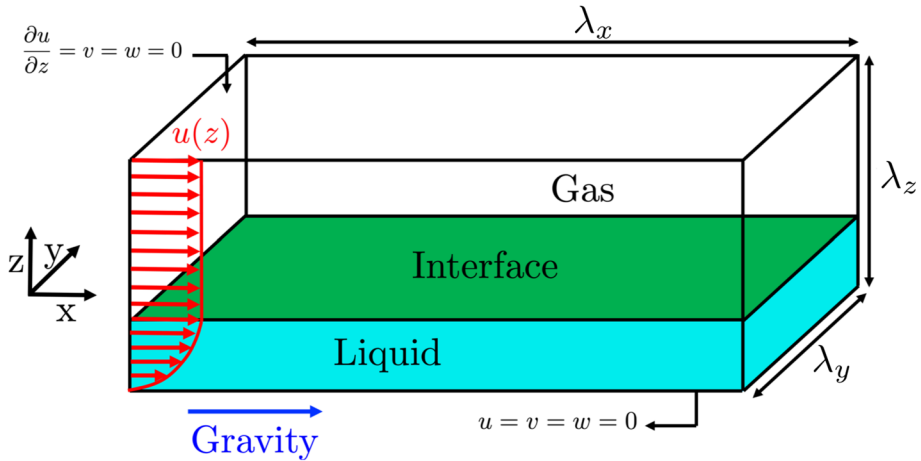


**Fig. 1** A classical computational domain of a three-dimensional falling film configuration and its appropriate boundary conditions

where  $\mathbf{F}_L$  and  $\mathbf{G}$  are given by:

$$\mathbf{F}_L = \int \sigma \kappa_f \mathbf{n}_f \delta_f(\mathbf{x} - \mathbf{x}_f) ds \quad \text{and} \quad \mathbf{G} = \int \mathbf{n}_f \delta_f(\mathbf{x} - \mathbf{x}_f) ds \quad (5)$$

Here  $\mathbf{x}_f$  is the parametrization of the interface while  $\delta_f(\mathbf{x} - \mathbf{x}_f)$  is the three-dimensional Dirac function which is non-zero only for  $\mathbf{x} = \mathbf{x}_f$ . Finally,  $\mathbf{n}_f$  is unit normal vector and  $ds$  is the length of the Lagrangian interface element.

To calculate interface motion:

$$\mathbf{V} = \frac{d\mathbf{x}_f}{dt}. \quad (6)$$

The Lagrangian interface  $\mathbf{x}_f$  is advected by integrating the equation above with a second order Runge–Kutta method where the interface velocity,  $\mathbf{V}$ , is interpolated directly from the Eulerian velocity. Physical properties e.g. density  $\rho$  and viscosity  $\mu$  are defined in the entire domain using the Heaviside indicator function  $\mathcal{H}(\mathbf{x}, t)$  as:

$$\begin{aligned} \rho(\mathbf{x}, t) &= \rho_a + (\rho_l - \rho_a) \mathcal{H}(\mathbf{x}, t) \\ \mu(\mathbf{x}, t) &= \mu_a + (\mu_l - \mu_a) \mathcal{H}(\mathbf{x}, t) \end{aligned} \quad (7)$$

where the subscripts  $a$  and  $l$  designate the air and liquid phases, respectively (see Table 1 for their values).

The initial condition for the velocity is set as a parabolic velocity profile in the liquid phase and determined from the well known Nusselt theory [30]:

$$u(z) = \frac{\rho_l g \sin(\beta)}{\mu_l} z \left( h_N - \frac{z}{2} \right) \quad (8)$$

**Table 1** Physical parameters used in this study

Variables	Notation	Value/range	Unit
Substrate inclination angle	$\beta$	$\pi/2$	rad
Liquid viscosity	$\mu_l$	$3.13 \times 10^{-3}$ and $10^{-3}$	Pa s
Liquid density	$\rho_l$	1098.3, 997, and 1000	kg m <sup>-3</sup>
Air viscosity	$\mu_a$	$1.81 \times 10^{-5}$	Pa s
Air density	$\rho_a$	1.125	kg m <sup>-3</sup>
Surface tension	$\sigma$	0.0484 and 0.072	N/m
Gravitational acceleration	$g$	9.81	m/s <sup>2</sup>
Nusselt film thickness	$h_N = \left( \frac{3\mu_l^2 Re}{\rho_l^2 g \sin(\beta)} \right)^{1/3}$	334.0, 243.6, and 313	μm
Film Reynolds number	$Re = \frac{\rho_l u_N h_N}{\mu_l}$	15, 59, and 100	–
Kapitza number	$Ka = \frac{\sigma}{\rho_l^{1/3} (g \sin(\beta))^{1/3} \mu_l^{4/3}}$	509.5, 3923, and 3363	–

where  $\beta$  is the angle of inclination (fixed here to  $\pi/2$  rad), and  $h_N$  the initial liquid thickness which is also deduced from Nusselt theory:

$$h_N = \left( \frac{3\mu_l^2 Re}{\rho_l^2 g \sin(\beta)} \right)^{1/3}. \quad (9)$$

This condition satisfies the no-slip boundary condition  $u(z=0) = 0$  at its lower boundary. In the air phase, the velocity is initialised with a constant value  $u_N$  representing the the Nusselt velocity value at the interface  $z = h_N$  (see its definition in Table 1). Thus at the top boundary  $z = \lambda_z$ , a stress-free condition is applied:

$$\frac{\partial u}{\partial z} = v = w = 0 \quad (10)$$

Finally, the temporal integration scheme used in this study is based on a second-order GEAR method, with implicit solution of the viscous terms of the velocity components. The time step  $\Delta t$  chosen at each temporal iteration is sought to fulfill an adaptive minimization criterion shown below:

$$\Delta t = \min \{ \Delta t_{cap}, \Delta t_{vis}, \Delta t_{CFL}, \Delta t_{int} \} \quad (11)$$

where  $\Delta t_{cap}$ ,  $\Delta t_{vis}$ ,  $\Delta t_{CFL}$ , and  $\Delta t_{int}$  represent the capillary, the viscous, the Courant–Friedrichs–Lewy (CFL), and interfacial CFL time steps, accordingly. Each criterion is defined by the following bounds:

$$\begin{aligned} \Delta t_{cap} &\equiv \frac{1}{2} \sqrt{\frac{(\rho_a + \rho_l) \Delta x_{\min}^3}{\pi \sigma}}, & \Delta t_{vis} &\equiv \left( \frac{\rho_l}{\mu_l} \right) \frac{\Delta x_{\min}^2}{6} \\ \Delta t_{CFL} &\equiv \min \left( \frac{\Delta x_j}{u_j} \right), & \Delta t_{int} &\equiv \min \left( \frac{\Delta x_j}{||\mathbf{V}||} \right) \end{aligned} \quad (12)$$

where  $\Delta x_{\min} = \min_j(\Delta x_j)$  refers to the minimum size  $x$  of a given cell  $j$ ,  $u_j$  and  $\mathbf{V}$  are the fluid and interface velocities, respectively.

### 3 Results

As highlighted in the introduction section, only a few studies have focused on full 3D falling waves, but not for a Reynolds number higher than 59. Here we simulate three distinct cases defined by small, moderate, and high Reynolds number regimes (15, 59, and 100). Even though these three values of Reynolds number are above the stability threshold, the small ( $Re = 15$ ) and the moderate ( $Re = 59$ ) cases do not easily reach a three-dimensional steady state if the interface is initially flat. In order to accelerate the development of these waves, it is possible to excite the inlet flow with a temporal pulsation (similar to the experiments of Park and Nosoko [32]). However, the introduction of this type of temporal excitation will require a very long domain length in the streamwise direction. Therefore, we restrict the domain size  $\lambda_x \times \lambda_y \times \lambda_z$  to a minimum periodic domain encompassing only a single wave. The idea is to set the interface with an initial perturbation in both the streamwise and the spanwise directions (a similar approach was used by Batchvarov et al. [9] and Dietze et al. [18]) with the following formulation:

$$h(x, y) = h_N \left[ 1 + 0.2 \cos \left( \frac{2\pi x}{\lambda_x} \right) + 0.05 \cos \left( \frac{2\pi y}{\lambda_y} \right) \right] \quad (13)$$

where  $h_N$  refers to the Nusselt film thickness defined in Table 1. Moreover, the value of  $\lambda_x$  is chosen carefully by taking into account the temporal frequency of pulsation and the Nusselt velocity  $u_N$  (the velocity of the interface). As for the length in the spanwise direction  $\lambda_y$ , this value is also chosen in order to mimic experimental setups using needles arranged at equidistant values (see Park and Nosoko [32] for experimental details). This type of setting is used only for  $Re = 15$  and 59. The case with  $Re = 100$  represents the major novelty of this study as it will require no initial deformation. The values of  $\lambda_x$ ,  $\lambda_y$ , and  $\lambda_z$  for all cases are provided in Table 2.

Figure 2 highlights the temporal evolution of the waves for the case defined by  $Re = 15$ , starting from its initial state ( $t = 0$  s) until reaching a steady state ( $t \sim 0.27$  s) where the waves do not evolve further. The initial perturbation remains the largest wave throughout its entire development. Several capillary waves grow in front of the principal wave with almost the same shape but smaller in amplitude. In this example, we can notice the importance of the initial perturbation for both the  $x$ - and  $y$ -directions defined in Eq. (13). If the initial perturbation was set only in the streamwise,  $x$ -direction, we would have expected a two dimensional wavy outcome for a while before a second bifurcation toward a three-dimensional wavy outcome. Therefore this initial perturbation in both  $x$ - and  $y$ -directions enable the calculation to speed-up towards the final three-dimensional steady outcome

**Table 2** Domain size for each of the three cases in this study, where the units are in millimeters (mm), and the resolution used for each case

$Re$	$Ka$	$\lambda_x$	$\lambda_y$	$\lambda_z$	$N_x \times N_y \times N_z$
15	509.5	20.7	20.7	1.2	$768 \times 768 \times 64$
59	3923	25	20	1.2	$1152 \times 768 \times 64$
100	3363	80	50	2.0	$2304 \times 1536 \times 128$

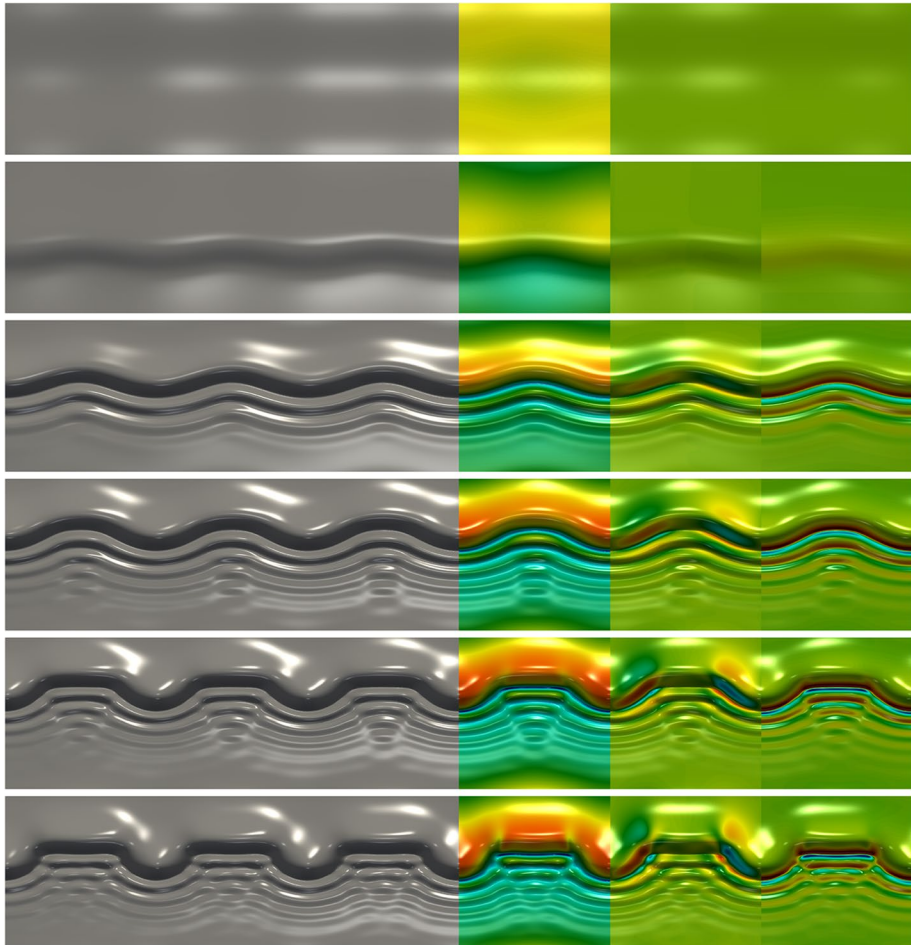


**Fig. 2** Temporal evolution wave in a minimum periodic domain  $\lambda_x = \lambda_y = 20.7$  mm,  $\lambda_z = 1.2$  mm for  $Re = 15$ ,  $Ka = 509.5$ . With a panel from top to bottom correspond to the time  $t = 0, 0.03, 0.09, 0.15, 0.21$ , and  $0.27$  s respectively. The last three columns are colored with the velocity components  $u, v$ , and  $w$  respectively

represented in Fig. 2 for  $t = 0.27$  s. It is fair to say, through this first example represented in Fig. 2, that computations of three-dimensional falling film do not require complex numerical methods that account for interfacial singularities (pinchoffs or coalescences). Instead, they require particular attention to their initialisations otherwise the computations will take a lot of time to reach a fully three-dimensional steady outcome.

Figure 3a shows a three-dimensional view of a single wave for  $Re = 15$  highlighting two slices in the  $x$ - $z$  plan. At this range of small Reynolds number, these two slices are similar but shifted in the  $x$ -direction. The red-slice at the edge of the domain (see Fig. 3a) and the blue-slice in its middle can be superposed to each other. In the Fig. 3b, we have isolated the red one slice and shown the flow structure inside the liquid layer. Here, the streamlines are obtained in the frame of reference of the moving wave. Therefore, a re-circulation zone is depicted in the top of the highest wave. In Fig. 3c, we



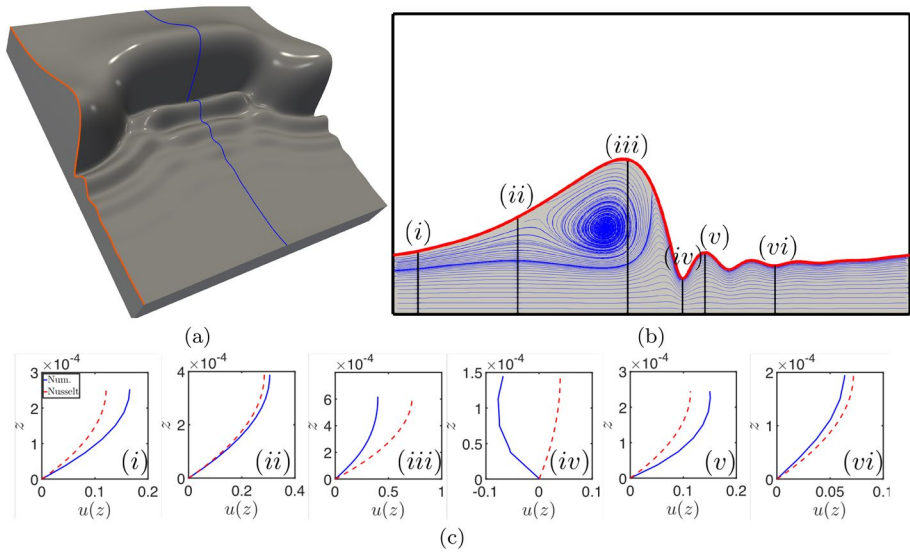


**Fig. 3** Left: Three-dimensional view of a single wave with similar properties as in properties as in Fig. 2. Right: A two-dimensional slice followed by some velocity profile compared with a classical Nusselt profile as in Eq. (8)

have plotted the parabolic velocity profiles at several  $x$ -positions, and compared with the theoretical Nusselt profile (Eq. 8). For some positions, the resulting velocity profile can be faster than local  $u_N$  (such as in positions (i), (ii), and (iii) of Fig. 3b, c), and for others it is the opposite. However, it is interesting to point out a counter intuitive phenomena which concerns the position where the interface high is at its minimum value (the position (iv)). The velocity profile at this position is negative, which means that the flow is locally reversed, and contributes to keep the wave behind it always high (the position (iii)). A final remark for this case is the value of its initial Nusselt high (for  $Re = 15$ )  $h_N = 334 \mu\text{m}$  which is larger than  $h_N$  values for both cases  $Re = 59$  and  $100$ . This is due to the liquid viscosity which is three times higher. The reason of choosing such a choice is to highlight that even for very thick initial liquid high, the flow can behave in a laminar regime. In nature, we can observe smooth and laminar falling films with very thick liquid layers, for example the flow of thick volcanic lava falling downward on rocks which is very laminar, compared to thin water which is very wavy (Fig. 4).

The next example we show in this section is the case of  $Re = 59$  where the properties of the liquid are similar to the those of pure water. We use this example to show more complex and regular shape of waves and also as a validation comparing to experimental work of Park and Nosoko [32]. This configuration has also been investigated by Sheid et al. [34], Dietze et al. [17, 18], and recently in Batchvarov et al. [9], where similar patterns were observed. Thus, we focus on the latest snapshot and perform a fast Fourier transform (FFT) on its interface shape. Taking into account the last known state of the CFD results and making use of the double periodic profile, the interface height profile,  $h(x, y)$ , was decomposed into spatial Fourier modes as follows:



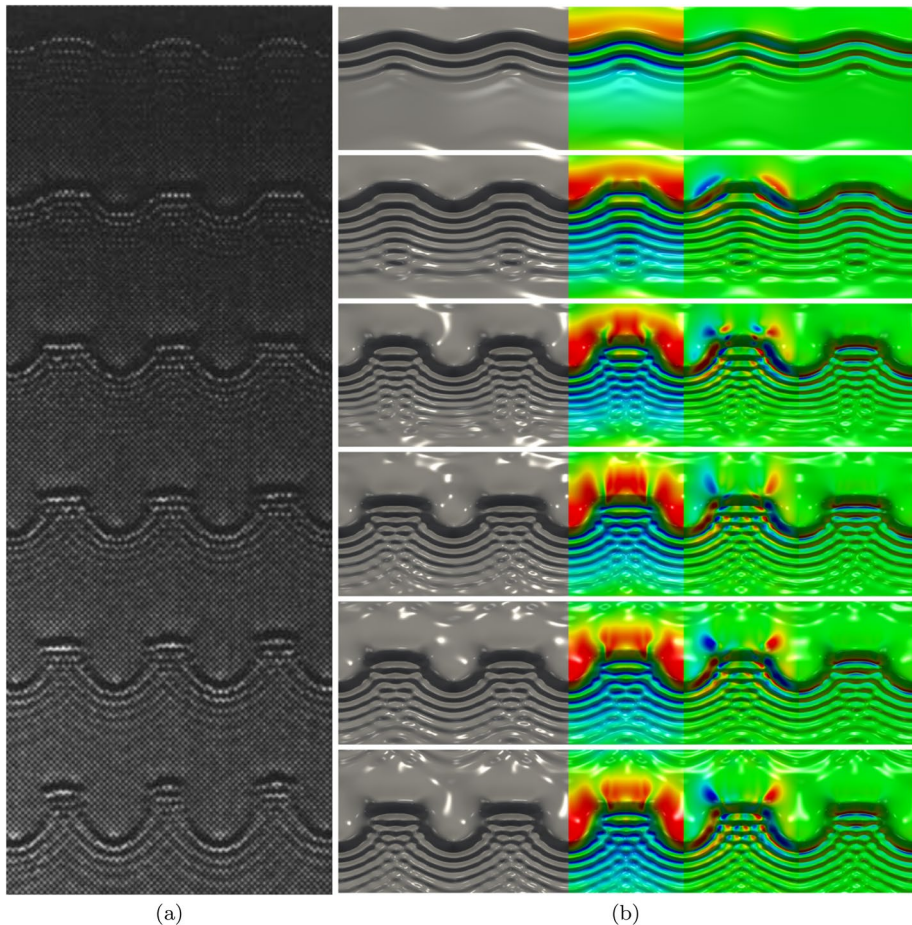


**Fig. 4** **a** Experimental snapshot from Park and Nosoko [32] and **b** simulation results for falling film refined by  $Re = 59$ . The times associated with panel **(b)** from top to bottom are:  $t = (0.067, 0.13, 0.19, 0.25, 0.31, 0.37)$  s, respectively

$$h(x, y) - h_N(x, y) = \sum_{(m,n)=-\infty}^{\infty} \zeta_{(m,n)} e^{i\left(\frac{2\pi}{\lambda_x}mx + \frac{2\pi}{\lambda_y}ny + \phi_{(m,n)}\right)}, \quad (14)$$

where  $m$  and  $n$  are the wave numbers for the  $x$ - and  $y$ -direction, respectively. Moreover, the FFT coefficients for each mode are given by the amplitude  $\zeta(m, n)$ . The characteristics of these coefficients are  $\zeta_{(0,0)} = 0$  and all symmetrical modes are equals ( i.e.  $\zeta_{(-m,n)} = \zeta_{(m,-n)} = \zeta_{(-m,-n)} = \zeta_{(m,n)}$ ). The analysis goes on to perform a number of interface reconstruction using 4, 10, 20, and 30 spectrum-modes respectively. Since the amplitudes  $\zeta(m, n)$  are symmetric we have the 15 coefficients necessary for our reconstruction, provided in Table 3.

Figure 5a depicts the relative height of the interface  $(h(x, y) - h_N)$  obtained from CFD, where Fig. 5b shows its spatial spectrum. Inside this spectrum, we have highlighted, through colored squares, the different spectrum modes used for the reconstruction of the

**Table 3** Spectrum coefficient  $\zeta_{m,n}$  resulting from FFT and used for reconstructing analytically the wavy as in Fig. 5f

$m/n$	0	1	2	3	4	5	6	7
0	0	4.61E-1	9.60E-2	1.08E-1	9.72E-2	4.32E-2	1.87E-2	3.45E-2
1	1.09E-1	1.73E-1	1.66E-1	7.00E-2	1.79E-2	4.76E-2	3.93E-2	1.61E-2
2	6.38E-2	5.22E-2	5.84E-2	4.02E-2	2.69E-2	1.16E-2	1.81E-2	2.39E-2
3	6.06E-3	1.41E-2	2.30E-2	3.63E-2	2.93E-2	1.66E-2	1.16E-3	1.12E-2
4	4.41E-4	7.21E-4	4.74E-3	9.39E-3	1.46E-2	1.67E-2	1.24E-2	7.58E-3
5	2.16E-3	2.97E-3	5.37E-3	8.61E-3	1.03E-2	9.36E-3	9.03E-3	4.67E-3
6	1.53E-4	3.79E-4	2.21E-3	5.28E-3	8.70E-3	1.13E-2	1.23E-2	1.13E-2
7	9.65E-5	3.83E-4	7.41E-4	1.53E-3	3.20E-3	5.09E-3	7.64E-3	8.86E-3
8	1.44E-4	3.12E-4	5.38E-4	1.11E-3	1.57E-3	1.46E-3	1.57E-3	2.40E-3
9	2.52E-4	3.44E-4	4.63E-4	4.82E-4	6.89E-4	1.11E-3	1.37E-3	1.38E-3
10	3.38E-4	4.44E-4	5.00E-4	4.15E-4	2.50E-4	2.94E-4	4.57E-4	6.09E-4
11	4.84E-4	3.76E-4	1.89E-4	1.89E-4	1.35E-4	1.61E-4	2.66E-4	3.98E-4
12	1.09E-4	1.17E-4	4.83E-5	5.42E-5	1.06E-4	1.48E-4	1.89E-4	2.74E-4
13	2.76E-5	5.20E-5	7.86E-5	9.79E-5	1.06E-4	1.12E-4	1.31E-4	1.64E-4
14	1.90E-5	4.00E-5	6.99E-5	8.52E-5	9.16E-5	9.09E-5	8.18E-5	7.53E-5
15	1.05E-4	9.99E-5	8.13E-5	4.16E-5	1.29E-5	2.04E-5	3.10E-5	3.67E-5
$m/n$	8	9	10	11	12	13	14	15
0	2.98E-2	1.97E-2	1.04E-2	1.96E-2	2.59E-2	1.61E-2	9.10E-3	1.90E-2
1	1.14E-2	2.25E-2	2.29E-2	1.40E-2	7.20E-3	1.98E-2	2.01E-2	8.83E-3
2	1.51E-2	4.10E-3	1.16E-2	1.54E-2	1.64E-2	6.59E-3	6.94E-3	9.25E-3
3	1.32E-2	1.27E-2	5.54E-3	3.16E-3	9.65E-3	1.16E-2	8.45E-3	8.70E-3
4	5.62E-3	1.15E-2	7.21E-3	2.99E-3	7.99E-3	1.40E-2	9.60E-3	3.55E-3
5	4.94E-3	8.96E-3	7.70E-3	8.60E-3	9.19E-3	9.94E-3	9.17E-3	4.77E-3
6	9.44E-3	7.48E-3	7.15E-3	8.37E-3	7.49E-3	7.01E-3	5.90E-3	2.70E-3
7	9.43E-3	1.02E-2	9.52E-3	7.87E-3	5.27E-3	2.13E-3	2.20E-3	2.10E-3
8	3.02E-3	3.25E-3	3.11E-3	2.66E-3	2.37E-3	1.58E-3	5.44E-4	2.89E-4
9	1.23E-3	1.21E-3	9.98E-4	9.42E-4	9.76E-4	7.90E-4	5.21E-4	2.86E-4
10	6.20E-4	5.34E-4	5.05E-4	6.41E-4	7.97E-4	8.59E-4	8.25E-4	6.54E-4
11	5.49E-4	6.52E-4	5.84E-4	4.60E-4	4.52E-4	5.64E-4	6.75E-4	7.11E-4
12	3.86E-4	4.99E-4	5.60E-4	5.40E-4	4.70E-4	4.22E-4	4.66E-4	5.21E-4
13	2.36E-4	3.30E-4	4.15E-4	4.88E-4	5.27E-4	5.34E-4	5.37E-4	5.78E-4
14	1.02E-4	1.55E-4	2.05E-4	2.56E-4	3.07E-4	3.63E-4	4.17E-4	4.66E-4
15	3.84E-5	5.91E-5	8.77E-5	1.07E-4	1.22E-4	1.39E-4	1.71E-4	2.16E-4

interface. These squares (red, blue, green, and black) encompass 4, 10, 20, and 30 modes, and their contribution for the interface reconstruction are shown in Fig. 5c–f, respectively. Thus, the first 4 modes (inside the red-square) are able to build back the most dominant wave, where the blue square (10 modes) are not enough to depict accurately the capillary waves. Using 20 modes build an acceptable interface but a very accurate reconstruction requires larger number of spectrum mode, 30 modes, as in Fig. 5f.

In the final example, we discuss the propagation of natural and unexcited wave-forms on liquid film surfaces characterised by  $Re = 100$ . Contrary to the two previous

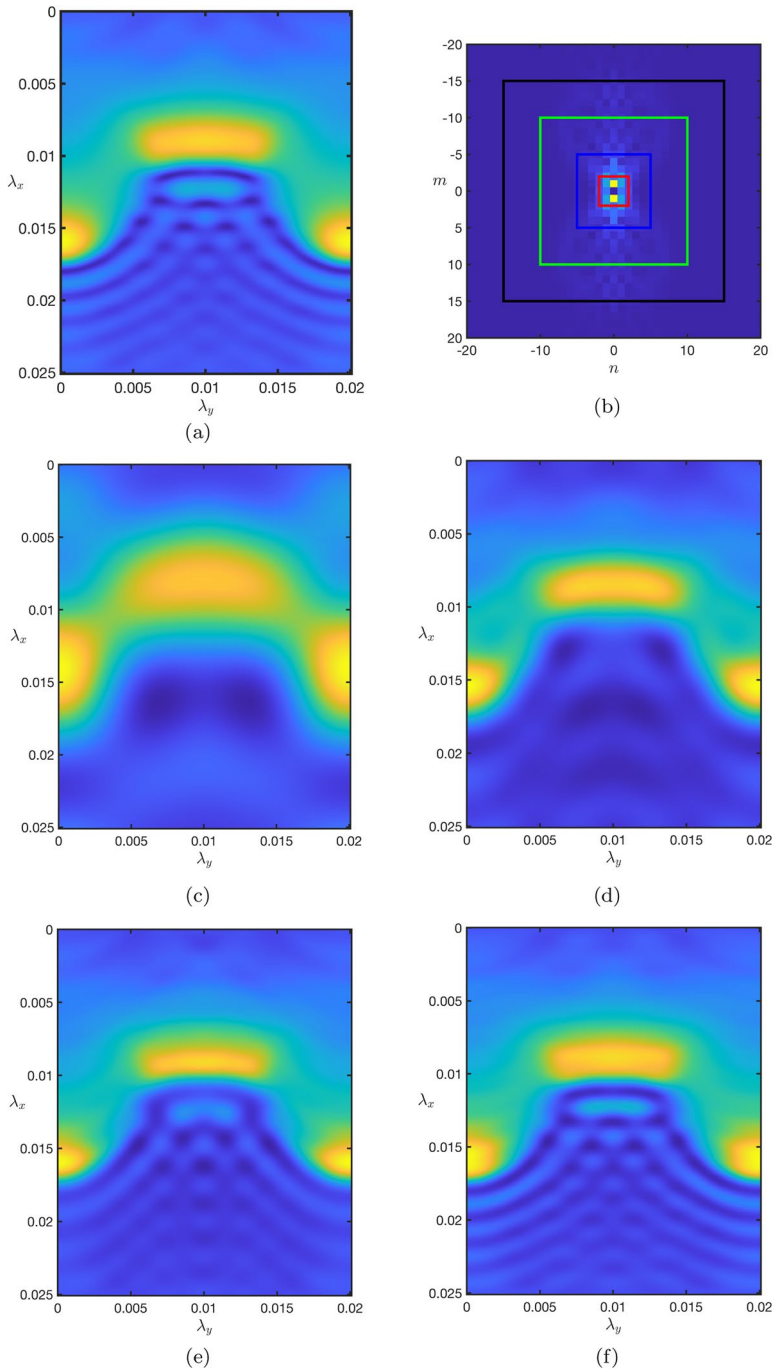
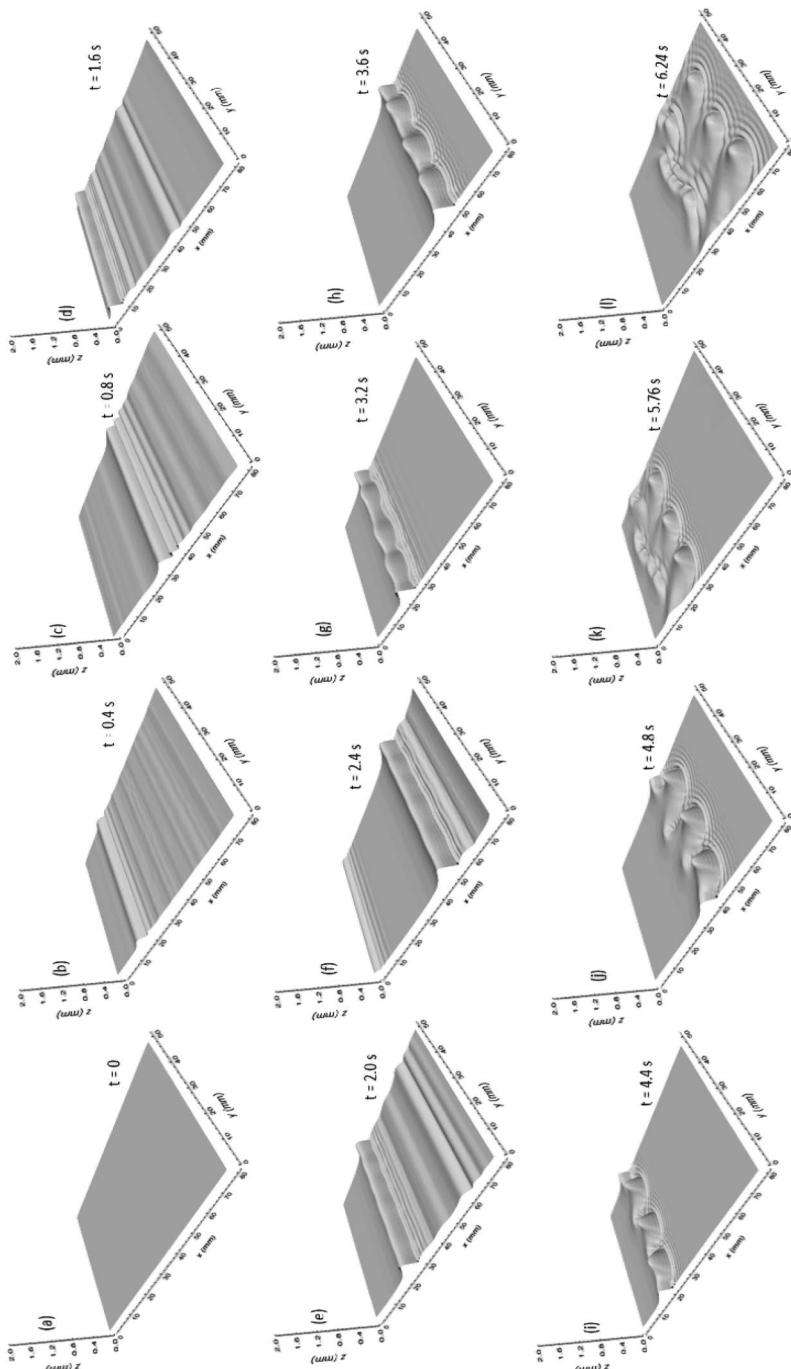


**Fig. 5** **a** The interface profile for the case  $Re = 59$  obtained directly from CFD at  $\tilde{t} = 330$  where all parameters remain unchanged from Fig. 4; **b** the spatial spectrum of CFD snapshot where the red, blue, green, and black square side lengths are 4, 10, 20, and 30 modes respectively; The reconstruction of the interface from Fourier modes in (c) red, (d) blue, (e) green, and (f) black squares respectively

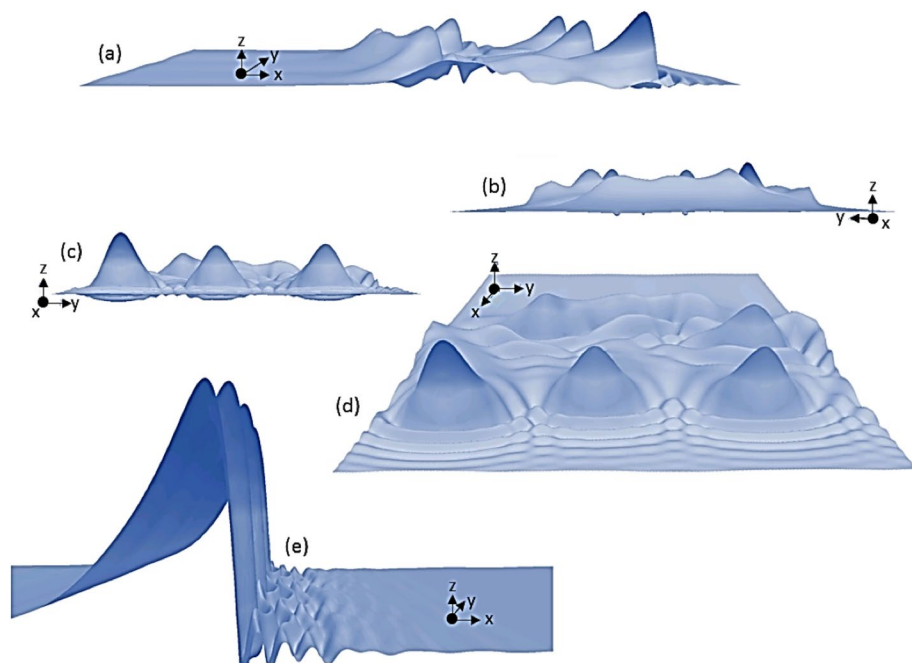
examples where the configuration consisted of mimicking a pulsed falling film type by setting the length of both the streamwise  $\lambda_x$  and spanwise  $\lambda_y$  directions in a minimum periodic domain, we have set a larger domain and let the interface falling naturally without any initial perturbation. Here, the interface height is set to  $h_N = 313 \mu\text{m}$ . As it has been widely reported and predicted in the literature [13, 22, 24], a natural propagation of waves on the film surface occurs when Reynolds number exceeds a critical value of  $Re_c = 5/4 \cot(\beta)$ . A primary instability is then excited by the amplification of infinitesimal disturbances. This primary instability is a convective instability type as it propagates downstream with the flow [2, 25]. Moreover, further downstream, this small amplitude noise-driven disturbances undergo exponential growth and then become visible. Then a transition into two-dimensional periodic waves appears and later the system develops solitary wave structures which are characterised by large-humped waves which are preceded by series of front running capillary waves. As these capillary waves interact with each other, the waves undergo inelastic collisions, with larger humped waves colliding and consuming the smaller humped waves. These wave harmonic interactions leads to the altering of the wave patterns, with the generation of three-dimensional structures on the film surface. Further downstream, the stability of the waves becomes more affected leading to the generation of highly asymmetric, three-dimensional and spatio-temporally unpredictable nonlinear waves covering the entire film surface [2, 16, 25].

Figure 6 shows the interface profile for the propagation of naturally developing waves on a film surface. The initial film corresponds to  $Re = 100$  and the substrate inclination is also considered as vertical ( $\beta = \pi/2$  radian). As shown in Fig. 6b, the first visible wave development starts with a two-dimensional periodic wave which appears on the film surface at  $t = 0.4$  s. These waves slowly propagate while more capillary structures develop in the front ( $t = 0.4$ – $2.0$  s). Subsequently, series of wave interaction are observed which lead to the growth of the wave hump as the waves propagate downstream. As the interaction process continues, the waves begin to yield to a three-dimensional instability type (see Fig. 6g for  $t = 3.2$  s), which modulates the waveform transversely thereby leading to the onset of three-dimensional structures on the film. These are well captured here due to our three-dimensional numerical framework. Essentially, curves are observed to form, which bulge downward and later expand into horseshoe structures. The legs of these structures further straighten upwards and aid to reduce the width of the flat parts. Finally, these horseshoes get detached from the flat parts and form a cluster of dimples on the film surface (see Fig. 6l for  $t = 6.24$  s). It must be noted that the solitary waves observed in this example (in contrast to those with smaller  $Re$ ) are characterised by irregular spacing due to the noise amplification. As a result, they tend to yield more easily to three-dimensional instabilities, which modulates the wave profile transversely. Finally, the solitary waves observed here are also characterised by large solitary humps, preceded by series of front-running capillary waves and succeeded by a long flat tail which confirms qualitative information about naturally developing waves [15, 26, 28, 32].

Figure 7 is basically a duplication of Fig. 6l with many view angles and highlights the unique features of its three-dimensional structure. It can be seen that these disordered three-dimensional waves show interesting features of curly and bulging horseshoe structures which possess sorts of spikes at the wave hump and a succeeding flat tail that extends to the developing Nusselt film. The miniature size of the preceding capillary ripples are also well-captured with details of the effect of the spanwise instability on the capillary structures also shown.



**Fig. 6** Time-propagation of naturally developing waves, in three dimensions. Simulation parameters are  $Re = 100$  and  $\beta = \pi/2$ . The interface height has been magnified 10 times to clearly reveal the wave propagation



**Fig. 7** Typical interface profile of disordered three-dimensional solitary waves on a flowing liquid film. Here, the interface height has been magnified 30 times to clearly reveal minutes details of the wave features

## 4 Conclusions and perspectives

The occurrence of falling films in a wide range of industrial, daily-life, and environmental applications has driven significant interest in the literature and has led to comprehensive reviews [12, 16, 22, 31]. We have presented full Direct Numerical Simulations of three-dimensional falling liquid films using a hybrid front-tracking/level-set method for tracking the interface. This method has the advantage of capturing many interfacial details with complex topology. Three cases have been presented with small, moderate and large Reynolds numbers. It is able to mimic a pulsed falling film type by setting a computational domain to a minimum wave length for both the streamwise and the spanwise direction. We have also demonstrated our capability of depicting the natural development of waves from a flat interface toward complex three-dimensional and disordered structures; these contain large solitary humps between front-running capillary waves and a long flat tail upstream. These types of features could not be predicted by a two-dimensional numerical framework.

This study also shows that it is possible to provide accurate predictions of three-dimensional falling films. In nature, the rheology of the liquid is not always Newtonian (such as mud or volcanic lava). It is time to move forward toward non-Newtonian falling film type, taking into account surface-active-agents (as additives or as contaminants), and perhaps taking into account energy equations with phase-changes as in the case of ice sheets.

**Acknowledgements** This work is supported by the Engineering and Physical Sciences Research Council, United Kingdom, through the EPSRC MEMPHIS (EP/K003976/1) and PREMIERE (EP/T000414/1) Programme Grants. O.K.M. also acknowledges funding from PETRONAS and the Royal Academy of



Engineering for a Research Chair in Multiphase Fluid Dynamics. We also acknowledge HPC facilities provided by the Research Computing Service (RCS) of Imperial College London for the computing time. D.J. and J.C. acknowledge support through computing time at the Institut du Développement et des Ressources en Informatique Scientifique (IDRIS) of the Centre National de la Recherche Scientifique (CNRS), coordinated by GENCI (Grand Equipement National de Calcul Intensif) Grant 2021 A0102B06721. The numerical simulations were performed with code BLUE (Shin et al. [35]) and the visualisations have been generated using ParaView.

**Open Access** This article is licensed under a Creative Commons Attribution 4.0 International License, which permits use, sharing, adaptation, distribution and reproduction in any medium or format, as long as you give appropriate credit to the original author(s) and the source, provide a link to the Creative Commons licence, and indicate if changes were made. The images or other third party material in this article are included in the article's Creative Commons licence, unless indicated otherwise in a credit line to the material. If material is not included in the article's Creative Commons licence and your intended use is not permitted by statutory regulation or exceeds the permitted use, you will need to obtain permission directly from the copyright holder. To view a copy of this licence, visit <http://creativecommons.org/licenses/by/4.0/>.

## References

1. Adebayo I, Xie Z, Che Z, Matar OK (2017) Doubly excited pulse waves on thin liquid films flowing down an inclined plane: an experimental and numerical study. *Phys Rev E* 96(1):013118
2. Alekseenko SV, Nakoryakov VY, Pokusaev BG (1985) Wave formation on a vertical falling liquid film. *AIChE J* 31(9):1446–1460
3. Alekseenko SV, Nakoryakov VE, Pokusaev BT (1994) Wave flow of liquid films. Begel House, New York
4. Balmforth NJ, Burbidge AS, Craster RV, Salzig J, Shen A (2000) Visco-plastic models of isothermal lava domes. *J Fluid Mech* 403:37–65
5. Balmforth NJ, Provenzale A (2001) Geomorphical fluid dynamics. Springer, New York
6. Balmforth NJ, Craster RV, Toniolo C (2003) Interfacial instability in non-Newtonian fluid layers. *Phys Fluids* 15(11):3370–338
7. Balmforth NJ, Liu JJ (2004) Roll waves in mud. *J Fluid Mech* 519:33–54
8. Baral DR, Hutter K, Greve R (2001) Asymptotic theories of large-scale motion, temperature, and moisture distribution in land-based polythermal ice sheets: a critical review and new developments. *Appl Mech Rev* 54(3):215–256
9. Batchvarov A, Kahouadji L, Canstante-Amores CR, Norões Gonçalves GF, Shin S, Chergui J, Juric D, Craster RV, Matar Omar K (2021) Three-dimensional dynamics of falling films in the presence of insoluble surfactants. *J Fluid Mech* 906:A16
10. Benjamin TB (1957) Wave formation in laminar flow down an inclined plane. *J Fluid Mech* 2(6):554–573
11. Benney DJ (1966) Long waves on liquid films. *J Math Phys* 45:150–155
12. Chang H-C (1994) Wave evolution on a falling film. *Annu Rev Fluid Mech* 26:103–36
13. Chang H-C, Demekhin EA (2002) Complex wave dynamics on thin films. Elsevier, Amsterdam
14. Charogiannis A, An JS, Markides CN (2015) A simultaneous planar laser-induced fluorescence, particle image velocimetry and particle tracking velocimetry technique for the investigation of thin liquid-film flows. *Exp Thermal Fluid Sci* 68:516–536
15. Charogiannis A, Denner F, van Wachem BG, Kalliadas S, Markides CN (2017) A simultaneous planar laser-induced fluorescence, particle image velocimetry and particle tracking velocimetry technique for the investigation of thin liquid-film flows. *Phys Rev Fluids* 2(1):014002
16. Craster RV, Matar OK (2009) Dynamics and stability of thin liquid films. *Rev. Mod. Phys.* 81(3):1131
17. Dietze GF, Kneer R (2011) Flow separation in falling liquid films. *Front Heat Mass Transf* 2:7033001
18. Dietze GF, Wilko Rohlf K, Nährich R, Kneer R, Scheid B (2014) Three-dimensional flow structures in laminar falling liquid films. *J Fluid Mech* 743:75–123
19. Gao D, Morley NB, Dhir V (2003) Numerical simulation of wavy falling film flow using VOF method. *J Comput Phys* 192(2):624–642
20. Grothberg JB (1994) Pulmonary flow and transport phenomena. *Annu Rev Fluid Mech* 26:529–571
21. Grothberg JB, Jensen OE (2004) Biofluid mechanics in flexible tubes. *Annu Rev Fluid Mech* 36:121–147
22. Kalliadas S, Ruyter-Quil C, Scheid B, Velarde MG (2011) Falling liquid films. Springer, Berlin, p 176



23. Kapitza PL, Kapitza SP (1949) Wave flow of thin layers of viscous liquids. Part III. Experimental research of a wave flow regime. *Z Eksp Teoret Fiziki* 19:105–120
24. Kofman N, Mergui S, Ruyer-Quil C (2014) Three-dimensional instabilities of quasi-solitary waves in a falling liquid film. *J Fluid Mech* 757:854–887
25. Liu J, Gollub JP (1994) Solitary wave dynamics of film flows. *Phys Fluids* 6(5):1702–1712
26. Liu J, Schneider JB, Gollub JP (1995) Three-dimensional instabilities of film flows. *Phys Fluids* 7(1):55–67
27. Miyara A (1999) Numerical analysis on flow dynamics and heat transfer of falling liquid films with interfacial waves. *Heat Mass Transf* 35(4):298–306
28. Nosoko T, Yoshimura PN, Nagata T, Oyakawa K (1996) Characteristics of two-dimensional waves on a falling liquid film. *Chem Eng Sci* 51(5):725–732
29. Nosoko T, Miyara A (2004) The evolution and subsequent dynamics of waves on a vertically falling liquid film. *Phys Fluids* 16(4):1118–1126
30. Nusselt W (1916) Die oberflächenkondensation des wasserdampfes. *VDI Z* 60:541–546
31. Oron A, Davis SH, Bankoff SG (1997) Long-scale evolution of thin liquid films. *Rev Mod Phys* 69:931
32. Park CD, Nosoko T (2003) Three-dimensional wave dynamics on a falling film and associated mass transfer. *AIChE J* 49(11):2715–2727
33. Ramaswamy B, Krishnamoorthy S, Joo SW (1997) Three-dimensional simulation of instabilities and rivulet formation in heated falling films. *J Comput Phys* 131(1):70–88
34. Scheid B, Ruyer-Quil C, Manneville P (2006) Wave patterns in film flows: modelling and three-dimensional waves. *J Fluid Mech* 562:183–222
35. Shin S, Chergui J, Juric D (2017) A solver for massively parallel direct numerical simulation of three-dimensional multiphase flows. *J Mech Sci Technol* 31(4):1739–1751
36. Shkadov VY (1967) Wave flow regimes of a thin layer of viscous fluid subject to gravity. *Fluid Dyn* 2(1):29–34
37. Shyy W, Francis M, Udaykumar HS, N'dri N, Tran-Son-Tay R (2001) Moving boundaries in micro-scale biofluid dynamics. *Appl Mech Rev* 54:405–454
38. Xie Z, Pavlidis D, Salinas P, Percival JR, Pain CC, Matar OK (2016) A balanced force control volume finite element method for interfacial flows with surface tension using adaptive anisotropic unstructured meshes. *Comput Fluids* 138:38–50
39. Yih CS (1955) Proceedings of the second US congress on applied mechanics ASME. New York, pp 623–628
40. Yih CS (1968) Instability of unsteady flows or configurations Part 1. Instability of a horizontal liquid layer on an oscillating plane. *J Fluid Mech* 31(4):737–751
41. Yu H, Gambaryan-Roisman T, Stephan P (2013) Numerical simulations of hydrodynamics and heat transfer in wavy falling liquid films on vertical and inclined walls. *J Heat Transf* 135(10):101010

**Publisher's Note** Springer Nature remains neutral with regard to jurisdictional claims in published maps and institutional affiliations.